Supporting Information

Unravelling the Interfacial Charge Dynamics of Atomically Dispersed Nickel on Hematite {001} Photoelectrodes

Qingqing Li,[a] Haiyang Fu,[b] Jundie Hu,[a] Jiafu Qu,[a] Siyuan Miao[a], Yanjie Liu,[a] Wei Sun,[b] Chang Ming Li[a,b] and Xiaogang Yang*[a]

[a] *Institute of Materials Science and Devices, School of Material Science and Engineering, Suzhou University of Science and Technology, Suzhou, 215009, P.R. China.*

[b] *Key Laboratory of Laser Technology and Optoelectronic Functional Materials of Hainan Province, Key Laboratory of Functional Materials and Photoelectrochemistry of Haikou, College of Chemistry and Chemical Engineering, Hainan Normal University, Haikou 571158, P.R. China*

*Corresponding author.

E-mail address: xiaogang.yang@gmail.com, yangxg@usts.edu.cn

1. Materials

All chemicals were used as received without further purification. Fluorine-doped tin oxide (FTO) substrates (F-SnO_2, 7 Ω sq^{-1}; South China Xiangcheng Technology Co.) were ultrasonically cleaned in deionized water, ethanol, and acetone prior to use. Analytical grade reagents, including $FeCl_3 \cdot 6H_2O$ (99%, Alfa Aesar), $FeCl_2$(≥99.5%, Sinopharm), $NiCl_2 \cdot 6H_2O$ (≥98%, Sinopharm), ammonium hydroxide (AR, 25-28%, Sinopharm), sodium acetate ($C_2H_3O_2Na$, 99%, Macklin), ethanol (C_2H_5OH, ≥99.7%, Cadro), Sodium Citrate ($C_6H_5O_7Na_3$, 98%, Aladdin), and NaOH (≥98%, Titan Scientific) were obtained commercially. Deionized (DI) water with a resistivity of ≥18.2 MΩ·cm was used throughout all experiments.

2. Characterization Techniques

X-ray diffraction (XRD) patterns of the hematite films were recorded using a Bruker D8 Advance diffractometer with Cu Kα radiation (λ = 1.5418 Å) operated at 40 kV and 40 mA. UV-Vis absorption spectra were acquired with a Shimadzu UV-2600 spectrophotometer over a wavelength range of 300-700 nm. Surface morphology was examined using scanning electron microscopy (SEM, JEOL JSM-IT800) at an accelerating voltage of 15 kV, with elemental distributions analyzed via energy-dispersive X-ray spectroscopy (EDS) mapping. High-resolution transmission electron microscopy (HRTEM) and selected area electron diffraction (SAED) were performed using a Thermo Scientific Talos F200S S/TEM operating at 200 kV. Atomic force microscopy (AFM) measurements were conducted in both ScanAsyst and Kelvin probe force microscopy (KPFM) modes using a Bruker Dimension Icon system with appropriate ScanAsyst and SCM-PIT probes.

X-ray photoelectron spectroscopy (XPS) was performed using a Thermo Fisher Scientific K-Alpha system equipped with an Al Kα excitation (1486.6 eV) under 2×10^{-9} Pa, with the C 1s peak set at 284.8 eV as reference. Surface binding energies and chemical compositions were analyzed, with Ar^+ ion etching conducted at 1-minute intervals. Spectra were collected before/after each etching cycle, corresponding to an approximate etching depth of a few nanometers per minute.

The Ni contents on the AD-Ni modified hematite were investigated by ICP-MS technology under a detection of ppb level, where the samples (2.2-2.3 cm^2) were dissolved in acidic solution for 5 mL.

TSPV measurements were conducted using a capacitor-like setup comprising a nanosecond laser (YAG: Q-smart 450, 355 nm), a differential voltage preamplifier (x100, AMETEK 5186), and a TDS Tektronix 5054 oscilloscope (500 MHz).

Ultraviolet photoelectron spectroscopy (UPS) measurements were carried out under the same vacuum conditions using a He I excitation source (21.2 eV). Gold (Au) was used as a standard reference. The low-binding-energy cutoff near high-kinetic-energy (0 eV) corresponds to the Fermi level (for Au) or the valence band maximum (VBM) of the semiconductor, while the low-kinetic-energy cutoff (typically between 15-21 eV) is used to determine the work function.

IPCE measurements were carried out using a CIMPS-QE/IPCE system, under varying applied potentials while keeping all other conditions constant. Wavelength-modulated light (TLS 03 with UV source) in the range of 300-700 nm was used for excitation.

ECSA was estimated via cyclic voltammetry (CV) using a CH Instruments 760E potentiostat. Measurements were conducted in 1 M NaOH under dark conditions within a potential window (e.g., 0.9-1.5 V vs. RHE). CV curves were recorded at varying scan rates from 20 to 100 $mV \cdot s^{-1}$.

EIS measurements were conducted using the same three-electrode setup under both dark and illuminated conditions. Under dark conditions, EIS was measured at 1.5 V vs. RHE. Under illumination (UV LED, λ = 365 nm, 400 $W \cdot m^{-2}$), measurements were taken at 0.9 V vs. RHE. The frequency range spanned from 100 kHz to 0.1 Hz, with an AC amplitude of 5 mV.

3. Estimation of surface dopant coverage

For hematite samples prepared with 8 cycles of deposition, the amount of dopant incorporation is assumed to scale linearly with the number of deposition cycles. Based on this assumption, the dopant coverage is estimated as follows: The inelastic mean free path (IMFP) of Fe photoelectrons is approximately 2 nm [1, 2], corresponding to a detection depth of 3 times of IMFP (about 6 nm), equivalent to roughly 26 atomic layers of Fe in hematite. For Ni doping, a Ni/Fe atomic ratio of 0.02875% corresponds to approximately 0.75 monolayers (ML) of Ni coverage in the topmost layer for 8 deposition cycles. For samples with 4 deposition cycles (half of 8 cycles), the Ni coverage is estimated to be approximately 0.38 ML (38% of a monolayer). These estimates assume uniform dopant distribution within the detected depth and a linear relationship between deposition cycles and dopant incorporation.

4. Calculation of charge carrier transfer lifetime (τ_n)

The photogenerated charge (hole) lifetime τ_n can be determined from the open-circuit potential (OCP) transients using the following equation, as established in previous reports[3, 4]:

$$\tau_n = -\frac{k_B T}{e}\left(\frac{dV_{OC}}{dt}\right)^{-1} \quad (1)$$

where, k_B is the Boltzmann constant, T is the absolute temperature, e is the elementary charge, and dV_{OC}/dt represents the derivation of the OCP transient decay, respectively. This analysis allows for the quantification of carrier dynamics by correlating the decay rate of the photovoltage to the recombination and transfer kinetics at the photoanode/electrolyte interface.

4. Supplementary results

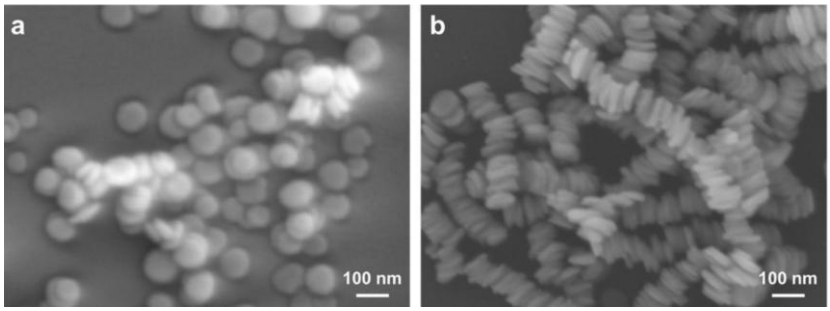

Fig. S1 SEM images of hexagonal hematite discs prepared by hydrothermal method. (a) discs lying on substrate, (b) discs packing. The thickness of the hematite discs was calculated to be 12-20 nm.

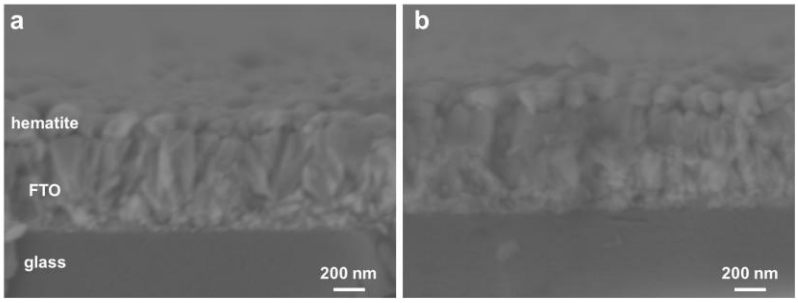

Fig. S2 Cross-sectional SEM images of (a) bare hematite and (b) AD-Ni modified hematite. Both films exhibit a consistent thickness of approximately 80 nm, confirming that the ultra-low concentration AD-Ni deposition does not alter the underlying hematite morphology or film thickness.

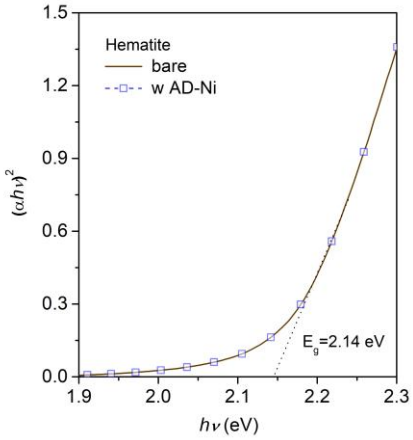

Fig. S3. Tauc plots hematite photoanodes with and without AD-Ni anchoring, direct bandgap model was applied.

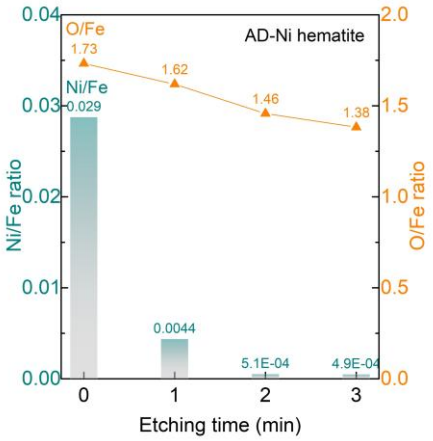

Fig. S4 XPS depth profile analysis of the AD-Ni modified hematite. Elemental depth profiles for Ni, Fe, and O obtained via Ar^+ etching. Based on an estimated etching rate of 1 nm/min, approximately 85% of the Ni atoms are localized within the topmost surface layer (<1 nm), confirming the surface-confined nature of the atomically dispersed Ni modification.

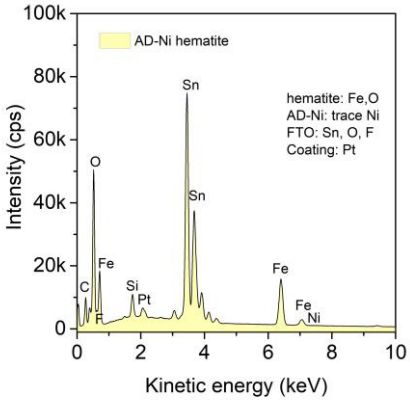

Fig. S5 EDS elemental analysis of the AD-Ni modified hematite film. Peak assignments confirm the presence of Fe and O from the hematite layer, as well as Sn, O, and F originating from the underlying FTO substrate. The Pt signal is attributed to the sputtered conductive coating applied for SEM imaging.

Table S1 ICP-MS of AD-Ni modified hematite films.

AD-Ni films	Ni (ppb)	Ni (ng/cm^2)	Ni atoms (nm^{-2})
2c	25.2	54.9	5.63
4c	43.1	98.0	10.05
8c	97.8	217	22.3

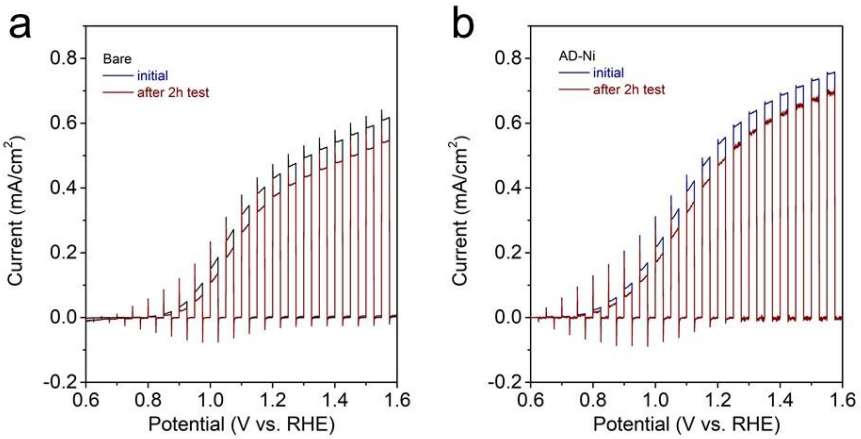

Fig. S6 J-V curves of the hematite photoanode after the stability test for 2 hours: (a) bare hematite; (b) AD-Ni modified hematite.

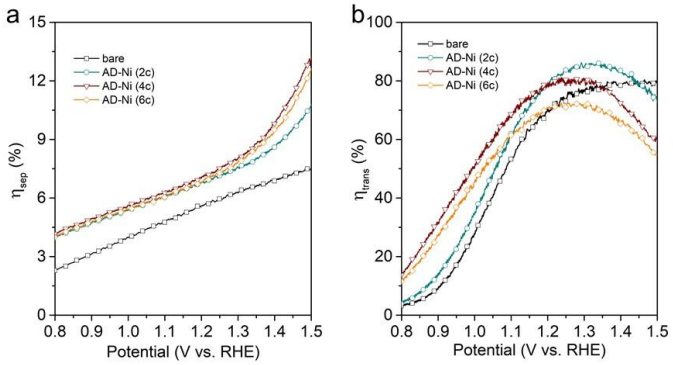

Fig. S7 Charge separation efficiencies (a) and transfer efficiencies (b) of hematite film w and w/o AD-Ni modification, 2-6 cycles of AD-Ni were employed. Sacrificial reagent (H_2O_2) was applied in 1 M NaOH for hole scavenge with assumed 100% charge transfer efficiencies.

Table S2 TOFs of bare and AD-Ni modified hematite photoanodes under various potentials.

Potential (V)	Bare (mA/cm^2)	AD-Ni (mA/cm^2)	Bare (nm^{-2})	AD-Ni (nm^{-2})	TOF (Bare)	TOF (AD-Ni)
0.9	0.026	0.105	1.619	6.573	0.178	1.621
1.1	0.192	0.324	11.985	20.248	1.315	3.723
1.3	0.405	0.483	25.285	30.164	2.775	4.197
1.5	0.507	0.566	31.640	35.313	3.473	4.542

Table S3. Semiconductor properties of the bare and AD-Ni modified hematite.

Parameter	Bare {001}	AD-Ni {001}	Functions of AD-Ni and Consistency
W_F (UPS) (eV)	4.91	4.88	Lower W_F,
V_{FB} (M-S) (V)	0.47	0.45	More Cathodic, matches W_F and V_{on}
E_{VBM}-E_F (eV)	1.97	1.94	E_F deeper in gap
E_{CBM} (eV)	4.82	4.76	Dipole at surface shifts band edge
E_{VBM} (eV)	6.88	6.82	Dipole at surface shifts band edge
V_{ph} (TSPV) (V)	0.160	0.237	Higher V_{ph}, enhanced separation or reduced recombination

Note: W_F, V_{FB}, E_{CBM}, E_{VBM}, V_{ph}, and V_{on} were work function, flat band potential, energy of conduction band minimum, energy of valence band maximum, photovoltage and onset potential of J-V curves, respectively.

Table S4 Parameters of equivalent circuits of bare and AD-Ni modified hematite from EIS.

Sample	Tech.	R_S ($ohm \cdot cm^2$)	R_{SC} ($ohm \cdot cm^2$)	C_{SC} ($F \cdot cm^{-2}$)	$R_{ct,trap}$ ($ohm \cdot cm^2$)	$C_{ct,trap}$ ($F \cdot cm^{-2}$)	Chi^2
Bare	EIS	6.70	3.01E+04	3.69E-06	2.61E+05	2.70E-06	0.043
AD-Ni	EIS	28.9	1.10E+02	2.65E-08	1.33E+05	3.57E-06	0.068
Bare	PEIS	9.06	3.34E+02	6.62E-06	5.27E+03	3.60E-05	0.022
AD-Ni	PEIS	5.14	1.97E+02	4.24E-06	8.42E+02	9.77E-05	0.019

Note: the electrochemical equivalent circuit was used as inset in Fig. 6b.

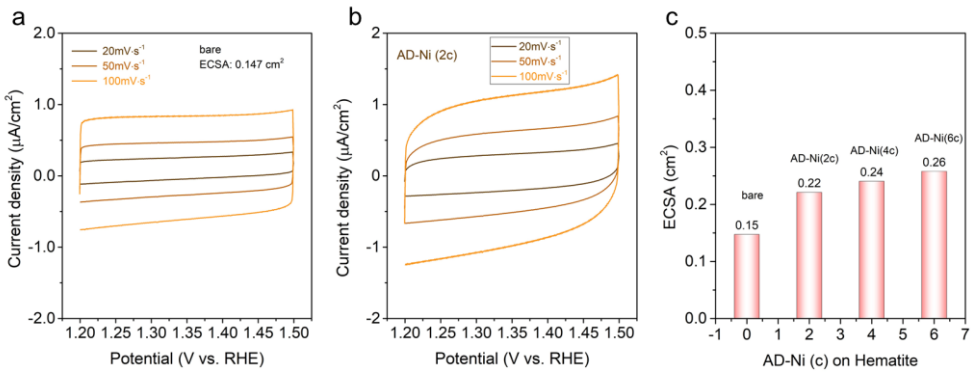

Fig. S8 CV curves of bare (a) and (b) AD-Ni modified hematite, (c) summarized ECSA with different cycles.

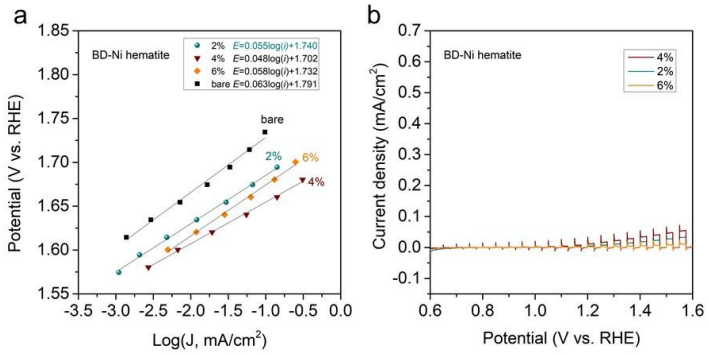

Fig. S9 Electrochemical characterization of bulk-doped Ni (BD-Ni) hematite films. (a) Tafel plots for the oxygen evolution reaction (OER) obtained under dark conditions for hematite films with Ni doping levels ranging from 2% to 6%. (b) Photocurrent density–potential curves under 365 nm LED illumination (400 W/m^2), illustrating the impact of bulk Ni incorporation on PEC water oxidation performance.

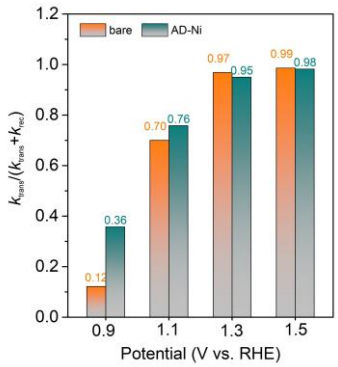

Fig. S10 Charge transfer efficiencies measured under various potentials for bare, AD-Ni modified hematite samples under various potentials, which were derived from the IMPS results.

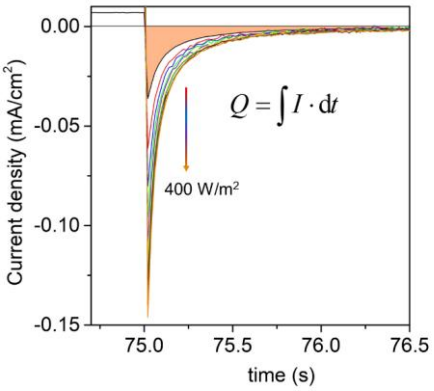

Fig. S11 Transient photocurrent responses under varied illumination intensities. The observed transient cathodic spikes (negative transients) upon switching the light source correspond to the back-flow of electrons recombining with surface-accumulated holes (h^+). The integrated area of these transients is directly proportional to the surface charge density (*Q*) trapped at the interface, reflecting the kinetics of hole accumulation and transfer.

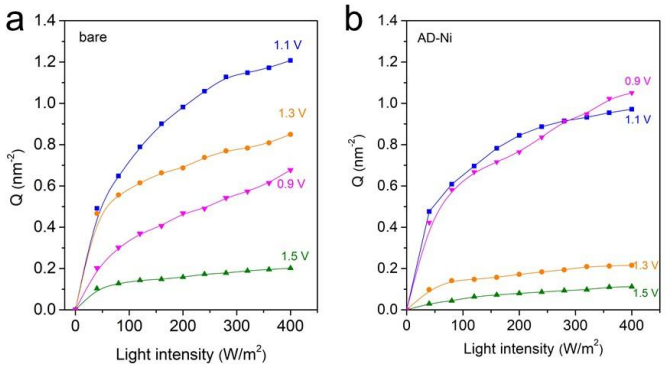

Fig. S12 Surface accumulated charge density Q under various applied potential: (a) bare hematite and (b) AD-Ni modified hematite measured across the potential range of 0.9-1.5 V vs. RHE. Increased illumination intensity results in a higher density of photogenerated surface holes. Notably, both samples exhibit a maximum in surface charge accumulation at ~ 1.1 V vs. RHE, representing the potential where the balance between hole generation and interfacial transfer kinetics is most prominent.

References:

[1] Shinotsuka, H.;Tanuma, S.;Powell, C. J.; Penn, D. R. Calculations of electron inelastic mean free paths. X. Data for 41 elemental solids over the 50 eV to 200 keV range with the relativistic full Penn algorithm. *Surf. Interface Anal.* **2015**, *47*, 871-888.

[2] Tanuma, S.;Powell, C. J.; Penn, D. R. Calculations of electron inelastic mean free paths. IX. Data for 41 elemental solids over the 50 eV to 30 keV range. *Surf. Interface Anal.* **2011**, *43*, 689-713.

[3] Zaban, A.;Greenshtein, M.; Bisquert, J. Determination of the Electron Lifetime in Nanocrystalline Dye Solar Cells by Open-Circuit Voltage Decay Measurements. *ChemPhysChem* **2003**, *4*, 859-864.

[4] Zhang, H.;Li, D.;Byun, W. J.;Wang, X.;Shin, T. J.;Jeong, H. Y.;Han, H.;Li, C.; Lee, J. S. Gradient tantalum-doped hematite homojunction photoanode improves both photocurrents and turn-on voltage for solar water splitting. *Nat. Commun.* **2020**, *11*, 4622.